




Blood flow efficiency in response to red blood cell sphericityMohammed Bendaoud ^{1,2,3,*} Mehdi Abbasi,^{2,4} Alexis Darras ¹ Hamid Ez-Zahraouy,³
Christian Wagner,^{1,5} and Chaouqi Misbah ^{2,†}¹*Dynamics of Fluids, Department of Experimental Physics, Saarland University,
66123 Saarbrücken, Germany*²*University of Grenoble Alpes, CNRS, LIPhy, F-38000 Grenoble, France*³*LaMCSel, URL-CNRST, Faculty of Sciences, Mohammed V University in Rabat 10000, Morocco*⁴*Aix Marseille Université, CNRS, Centre Interdisciplinaire de Nanoscience de Marseille (CINAM), Turing
Centre for Living Systems, 13009 Marseille, France*⁵*Department of Physics and Materials Science, University of Luxembourg, 1511 Luxembourg City,
Luxembourg*

(Received 9 December 2023; accepted 22 April 2024; published 10 May 2024)

The morphological properties of red blood cells, such as size and shape, play a crucial role in determining their flow properties. A typical abnormal shape can be found in several blood disorders, such as spherocytosis, ellipsocytosis, etc., where the cells have a spherelike or ellipselike appearance, instead of being biconcave. These shape anomalies can affect the ability of RBCs to deform and squeeze through narrow capillaries, leading to reduced blood flow and oxygen supply to tissues. This can cause tissue ischemia, which can lead to organ damage and dysfunction. We conduct numerical simulations in order to study the flow properties (such as flow rate, cell-free-layer, and RBCs hydrodynamic diffusion) by varying the shapes of the cells, from a biconcave one (healthy RBCs) to a spherical one, representing RBCs suffering spherocytosis disease. Our study highlights nontrivial effects, such as nonmonotonic behaviors of the flow rate as a function of asphericity, depending on the channel width. For example, for some channel width the usual biconcave shape is revealed to be optimal with respect to flow rate, whereas for other widths more inflated shapes are more efficient. This offers an interesting basis for the understanding of the mechanisms underlying blood flow deficiencies associated with shape anomalies, and may help evaluating the potential therapeutic strategies that might be used to alleviate the symptoms. As RBCs also serve as a classical model system for very deformable objects, our study reveals also some fundamental aspects of the flow of soft suspensions.

DOI: [10.1103/PhysRevFluids.9.053603](https://doi.org/10.1103/PhysRevFluids.9.053603)**I. INTRODUCTION**

Blood is a suspension of various components such as red blood cells (RBCs), white blood cells, and platelets suspended in an aqueous solution that contains proteins, organic molecules, and salts, called plasma. The RBCs constitute by far the major cellular components, so that the flow properties of blood (in a healthy situation) is determined by RBCs and plasma [1].

The shape and size of RBCs are important for their function [2]. In a healthy individual, RBCs are typically biconcave disks, which allows them to efficiently transport oxygen throughout the body.

*mohammed.bendaoud@uni-saarland.de

†chaouqi.misbah@univ-grenoble-alpes.fr

However, a number of abnormalities in RBCs morphology have been described [3,4]: spherocytes, elliptocytosis, schistocytes, stomatocytes, knizocytes, and mushroom-shaped cells.

Spherocytosis is an inherited disorder characterized by the presence of spherocytes in the blood. Spherocytes are RBCs that have a quasispherical shape. This abnormal shape makes them more prone to destruction in the spleen, resulting in hemolysis and anemia [5]. Elliptocytosis is another inherited disorder characterized by an elliptical RBC shape. Similar to spherocytosis, these RBCs are also more susceptible to destruction in the spleen [6].

Schistocytes correspond to RBCs that have a jagged or irregular shape, and can be caused by various conditions such as microangiopathic hemolytic anemia, disseminated intravascular coagulation, and thrombotic thrombocytopenic purpura [7]. Stomatocytes are RBCs that have a central depression or “open mouth” shape and can be caused by inherited conditions such as stomatocytosis [8]. Knizocytes are RBCs that have a crescent or “sickle” shape caused by sickle cell anemia [9]. Mushroom-shaped cells are RBCs that have a distinctive shape with a broad, flat top and a narrow, pointed bottom that can be caused by inherited conditions [4].

These RBC morphological anomalies can also be caused by exposure to certain drugs or chemicals [10]. Morphological changes in RBCs can be a useful diagnostic tool for identifying certain pathological conditions and understanding the underlying disease mechanisms [11].

Normally, RBCs have a high degree of deformability which plays an important role in blood flow, in particular in microcirculation [2,12–14]. There has been to date a large body of literature on the experimental and numerical studies of healthy RBCs shapes [15–36]. There have also been studies of binary suspensions, which reported that particle size and rigidity impact segregation in confined shear flow. Smaller particles and stiffer ones tend to localize near walls, while larger and flexible ones exhibit antimargination effect (localization of particles near the center), driven by size-dependent migration and rigidity-dependent collisions [37]. However, the effect of cell shape (e.g., like in spherocytosis and ellipsocytosis) on blood flow rheology remains a largely unexplored research area. The aim of this paper is to investigate the effect of abnormalities of RBCs morphologies on flow properties. We will explore several channel widths, and shapes and analyze systematically the flow properties for different hematocrits. We find a subtle behavior of the flow rate as a function of asphericity. For example, it is found that for some channel widths, the biconcave shape ensures a maximum RBCs transport, whereas for other widths, significantly more inflated cells prevail, or at least provide a similar flow rate as for the usual biconcave shape. We will analyze in a systematic way these behaviors, and provide some basic key elements to understand their origin.

II. METHODS

A. Mathematical and numerical models

The mathematical model and simulation method (based on the lattice Boltzmann method) have been described and validated in prior works [38–42]. The validation also involved a comparison with the boundary integral method [43]. For the sake of completeness, we present a brief summary here of the model. Figure 1 depicts RBCs immersed in a straight tube filled with a fluid mimicking plasma. We employ a 2D model for computational efficiency while maintaining the effectiveness of our model. Indeed, despite the reductionist nature of the 2D vesicle model, several analyses utilizing more sophisticated 3D models that incorporate the membrane cytoskeleton suggest that the simplified 2D vesicle model successfully captures several pivotal erythrocyte shapes and flow behaviors (like RBCs flow as a function of hematocrit) [44–48].

In Fig. 1, L and W are the channel length and width. The cell membranes are represented by symbol G , while the fluid domain is separated into Ω_{in} (inside the cells) and Ω_{ex} (outside the cells designating the “plasmic” domain). Cell coordinates are denoted by $\mathbf{X}(s)$, where s is the curvilinear coordinate (in 2D) along the cell membrane, with $s \in [0, P]$, where P is the cell perimeter.

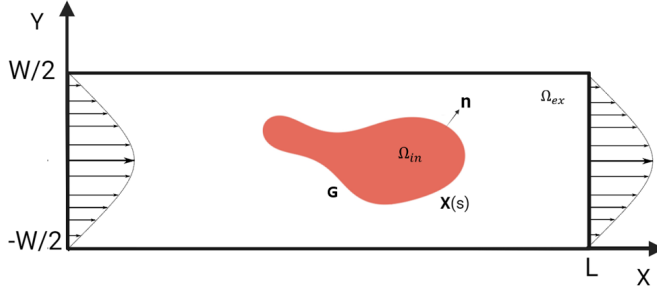


FIG. 1. A schematic representation of the studied configuration, wherein RBC is suspended in a straight channel filled with plasma. The channel dimensions are denoted by L and W , which correspond to the length and width, respectively. The fluid domains within and outside the cell are referred to as Ω_{in} and Ω_{ex} , respectively. The normal vector, denoted by \mathbf{n} , is directed outward, and the cell membrane is represented by the symbol G .

Under flow, the cell resists against deformation due to its membrane rigidity and inextensibility (in 2D). The corresponding bending energy (known as the Helfrich energy) is given by

$$\mathbf{H}(\mathbf{X}(s)) = \frac{\kappa}{2} \int_G c^2 ds + \int_G \zeta ds, \quad (1)$$

where κ is the bending rigidity modulus, c is the local curvature, and ζ is a Lagrange multiplier which enforces local membrane inextensibility. This energy leads to a restoring force (its expression is given below) of the membrane that is a function of local curvature c and its derivatives. The fluid inside and outside the cells obey the Navier-Stokes:

$$\rho \left(\frac{\partial \mathbf{u}}{\partial t} + \mathbf{u} \cdot \nabla \mathbf{u} \right) = -\nabla p + \nabla \cdot [(\mu/2)(\nabla \mathbf{u} + \nabla \mathbf{u}^T)] + \mathbf{f}, \quad \nabla \cdot \mathbf{u} = 0. \quad (2)$$

Here, ρ is the fluid density, μ is the dynamic viscosity, and \mathbf{f} is the force applied by the cell to the fluid. This force is obtained upon a functional derivative of the Helfrich energy and is given by [49]

$$\mathbf{f} = \kappa \left(\frac{\partial^2 c}{\partial s^2} + \frac{1}{2} c^3 - \zeta c \right) \mathbf{n} + \frac{\partial \zeta}{\partial s} \mathbf{t}. \quad (3)$$

Here \mathbf{n} and \mathbf{t} are the normal and tangential unit vectors, respectively, to the membrane, while $\mu(\mathbf{x})$ is the dynamic viscosity and has two different values within and outside the vesicle:

$$\mu(\mathbf{x}) = \begin{cases} \mu_{in} & \text{if } \mathbf{x} \in \Omega_{in} \\ \mu_{ex} & \text{if } \mathbf{x} \in \Omega_{ex} \end{cases}. \quad (4)$$

The above model equations are solved using the lattice Boltzmann method (LBM), combined with the immersed boundary method [39,40,50].

B. Simulation setup, dimensionless numbers, and definition of RBCs flux and effective viscosity

The suspension is subjected to a pressure gradient. This pressure gradient (actually, in LBM we apply a constant force on each lattice node) results in an undisturbed (i.e., in the absence of RBCs) Poiseuille flow $\mathbf{u}(u, v)$, and is given by

$$u = u_{\max} \left(1 - \frac{4y^2}{W^2} \right), \quad v = 0, \quad (5)$$

where u_{\max} is the maximal velocity at the center of the channel at $y = 0$.

TABLE I. The simulation's physical and dimensionless parameters.

Physical parameters	
Cell radius R_0 (μm)	2.7
Bending modulus κ (J)	$3 \cdot 10^{-19}$
Density ρ (Kg/m^3)	10^3
Plasma viscosity μ_{ex} ($Pa.s$)	10^{-3}
Dimensionless parameters	
Reynolds number Re	0.1
Capillary number Ca	18, 10, 0.2
Viscosity contrast λ	1, 6
Reduced area τ	From 0.45 to 0.99

Several dimensionless numbers can be defined to characterize this system:

(i) The capillary number, which is defined as the ratio of shear force to bending force

$$Ca = \frac{\mu_{ex} \dot{\gamma}_w}{\kappa} R_0^3, \quad (6)$$

where $\dot{\gamma}_w = \partial u_x / \partial y|_{y=-W/2}$ is the shear rate at the wall, $y = -W/2$, and R_0 is a characteristic radius of RBC (see below).

(ii) The degree of confinement

$$Cn = \frac{2R_0}{W}. \quad (7)$$

(iii) The viscosity contrast is the ratio between the viscosities of the internal and external fluids

$$\lambda = \frac{\mu_{int}}{\mu_{ext}}. \quad (8)$$

(iv) The reduced area (in 2D) corresponding to the degree of cell inflation (or asphericity)

$$\tau = \frac{4\pi A}{P^2}, \quad (9)$$

where P is the perimeter and A is the enclosed area of the cell. A healthy RBC has a reduced volume lying in the range 0.6 to 0.64. A RBC with a reduced volume of one corresponds to a sphere, close to a spherocyte. We will consider various reduced areas representative of several abnormal shapes such as those found, for example, in spherocytosis and elliptocytosis. In order to achieve a desired reduced area, we will modify the perimeter and fix the same area for all cells. Note that the reduced area of all cells remains constant. Later we will fix the perimeter and modify the area in order to explore the same range of reduced area. We will see that the overall picture remains unchanged whether the area or perimeter is fixed.

All typical values of physical parameters used in this study and the values of dimensionless parameters are given in Table I.

The LBM introduces naturally an inertial effect. However, the value of Reynolds number is typically 10^{-4} (see typical velocity in microcirculation in Table II), corresponding to a Stokes regime. This value is numerically too prohibitive (due to excessive computational time). Fortunately, several benchmarks have been established in the literature to identify a maximum value of Re below which the lattice-Boltzmann approach reproduces the Stokes regime with high precision. For the Stokes regime, there is general agreement that a value $Re = 0.1$ is a suitable balance between numerical efficiency and precision [38,39,51–53]. As a result, the Reynolds number in our simulation is set at a maximum of 0.1. A typical speed in microcirculation is in the range of mm/s, corresponding to a capillary number in the range 10–20. We will fix $Ca = 18$ in the main

TABLE II. Maximum flow velocity in the absence of cells in the channel center for different widths for $Ca = 18$ and its corresponding confinement.

Width	$W = 10 \mu\text{m}$	$W = 20 \mu\text{m}$	$W = 40 \mu\text{m}$
Maximum velocity (mm/s)	0.68	1.37	2.74
Cn	0.54	0.27	0.14

text and present the results corresponding to other values (10 and 0.2) in the Supplemental Material [54]. In the current study, we will explore values from 0.45 to 0.99 for the reduced area; the latter range corresponds to that found for red blood cells suffering spherocytosis. We explored different channel widths from $10 \mu\text{m}$ to $40 \mu\text{m}$. We use periodic boundary conditions along the flow direction. The length of the channel is taken to be large enough in order to avoid numerical artifacts due to periodic boundary conditions [55].

In this study we will analyze the cell flux across the flow direction as a function of (i) hematocrit, (ii) channel width, and (iii) reduced area. From the full suspension flux (flux of cells and the fluid) we can also extract the effective viscosity. It is defined as

$$\mu_{\text{eff}} = \frac{\mu_{\text{ex}} Q}{Q_{\text{ssp}}}, \quad (10)$$

where Q_{ssp} is the average flux of cell suspension, and Q is the flux of the pure plasma (with viscosity μ_{ex}) when subjected to the same pressure gradient.

More precisely, the blood volumetric flow rate ratio Q is calculated directly from the velocity:

$$Q(t) = \int_{\Gamma} (\mathbf{u}, \mathbf{n}) dy, \quad (11)$$

where Γ is a segment having length W and is perpendicular to the flow direction.

The flow rate in the absence of cells is calculated as

$$Q_0 = \frac{2}{3} W u_{\text{max}}. \quad (12)$$

The RBCs flow is calculated using the following equation:

$$Q_c = \frac{N_{\text{RBC}}}{T} A, \quad (13)$$

where N_{RBC} is the number of RBCs that cross the chosen section and T is the total time of the simulation.

III. RESULTS AND DISCUSSION

We explore different channel widths, where Table II shows the maximum flow velocity, in the absence of cells, for different channel widths, i.e., different confinement Cn . We will consider homogeneous suspensions, where each cell has the same given reduced area.

Below we will fix $Ca = 18$, and in the Supplemental Material we have included some results for different capillary numbers ($Ca = 10$ and $Ca = 0.2$) [54], as well as a different viscosity contrast of six, to ensure that we observe consistent behavior across the range of parameters (Ca and λ).

A. Red blood cells with fixed area

The change in area or volume of RBCs, due to diseases discussed above, will impact the reduced volume (in 3D) or reduced area (in 2D). Since our simulations concern 2D, we will explore different reduced areas, by first modifying the perimeter and fixing the enclosed area, and exploring the reverse situation in Sec. III B.

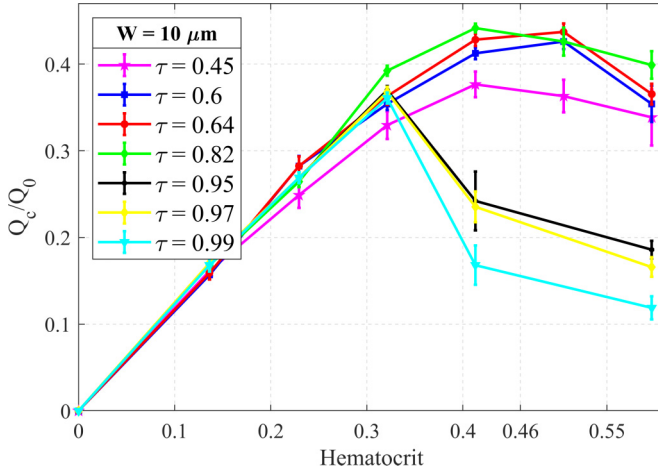


FIG. 2. Flux versus hematocrit for different reduced areas in a 10 μm ($Cn = 0.54$) channel width (RBCs with fixed area): A graphical representation of the relationship between flux and hematocrit for five distinct reduced areas (0.45–0.99). The total volume fraction ranges from 0 to 0.55, with a constant $Ca = 18$.

1. RBCs flux for different channel widths and different reduced area

In this section, our primary objective is to examine the impact of reduced area (by exploring different channel widths and hematocrits) on the flow properties of RBCs. We will first focus on the flux of RBCs.

Our findings, as illustrated in Figs. 2–5, show the intricate interplay between channel width and reduced area on blood flux optimization. Notably, those figures reveal that the attainment of the maximum blood flux is dependent on both the width of the channel and the specific reduced area value of the RBCs. For instance, our simulation data indicates that the highest blood flux is achieved at a reduced area of 0.82 when the channel width is maintained at 10 μm as shown in Fig. 2. A reduced area of 0.64 is associated with optimal blood flux in a channel with a width of 20 μm as

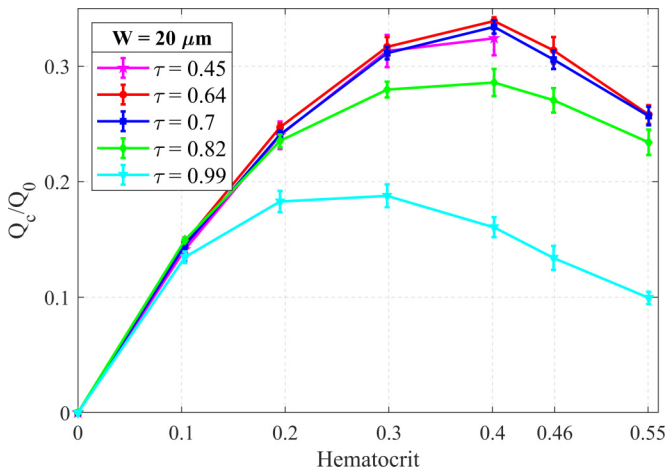


FIG. 3. Flux versus hematocrit for different reduced areas in a 20 μm ($Cn = 0.27$) channel width (RBCs with fixed area): A graphical representation of the relationship between flux and hematocrit for five distinct reduced areas (0.45, 0.64, 0.7, 0.82, and 0.99). The total volume fraction ranges from 0 to 0.55, with a constant $Ca = 18$.

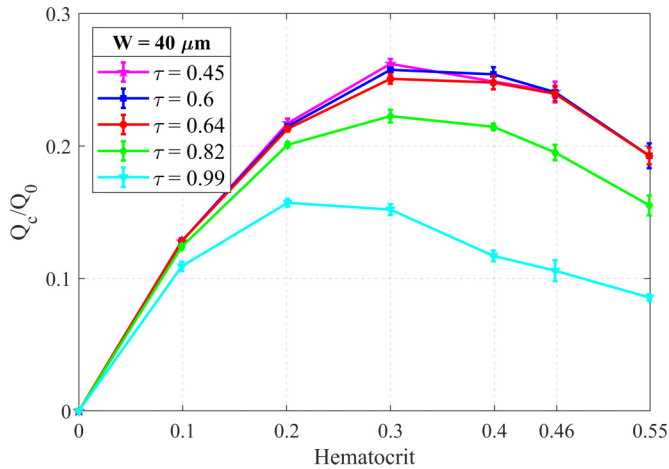


FIG. 4. Flux versus hematocrit for different reduced areas in a $40\ \mu\text{m}$ ($Cn = 0.14$) channel width (RBCs with fixed area): A graphical representation of the relationship between flux and hematocrit for five distinct reduced areas (0.45, 0.6, 0.64, 0.82, and 0.99). The total volume fraction ranges from 0 to 0.55, with a constant $Ca = 18$.

shown in Fig. 3, while a reduced area of 0.45 is found to be optimal in a channel with a width of $40\ \mu\text{m}$ as shown in Fig. 4. These observations highlight the nuanced relationship between channel dimensions and RBC morphology.

Some remarks are in order. As shown, for example, in Fig. 2, while the reduced area 0.82 seems to provide a higher flux than other reduced area, the differences in fluxes for reduced area 0.82, 0.64, and 0.6 are relatively small. We have repeated the simulation several times in order to rule out numerical errors, but the flux for reduced area 0.82 was always larger. Our results clearly show that in the case of spherocytosis (reduce area close to one; light blue line in Figs. 2–4) there is an important collapse of RBCs flux: the RBC flux is reduced by 25% up to about 50% in comparison to the flux in healthy conditions. When the reduced area is very high, indicating that RBCs are

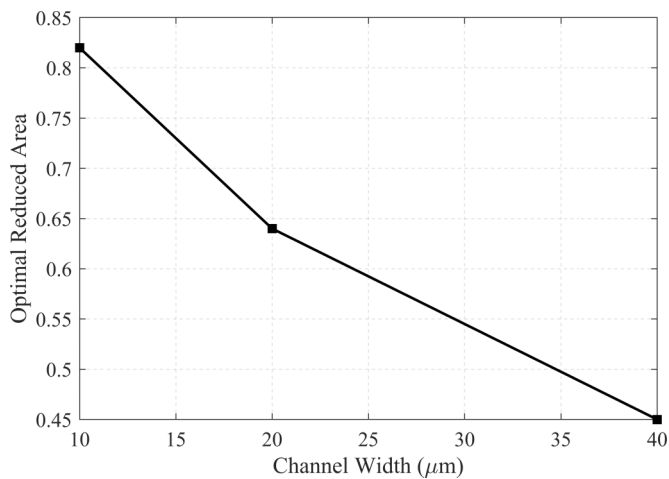


FIG. 5. Optimal reduced area of RBCs for maximum flow rate versus channel width: This figure illustrates the optimal reduced area of red blood cells (RBCs) where the highest flow rate is achieved (see corresponding figures of flux, Figs. 2–4) a function of the channel width (RBCs with fixed area).

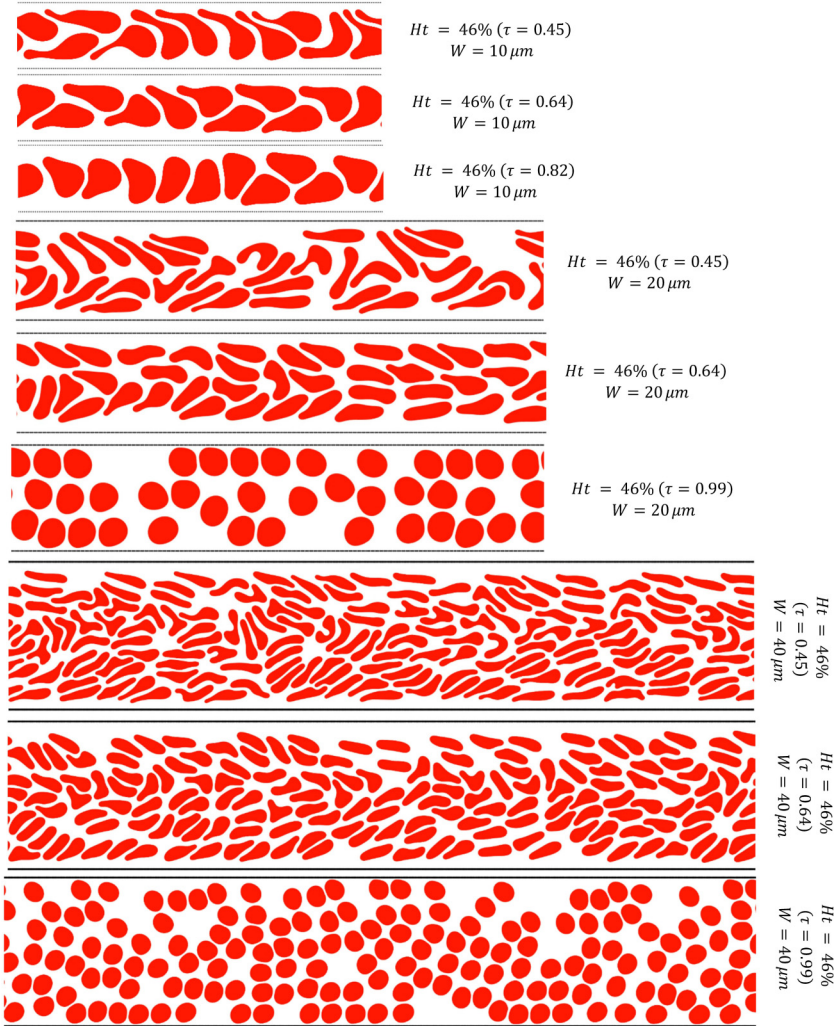


FIG. 6. Cell configurations for different selected channel widths and for different reduced areas.

nearly spherical, they may not deform adequately to navigate narrow channels efficiently (in Fig. 2 we see the same trend for reduced areas 0.95, 0.97, and 0.99). This results in increased resistance and a decrease in blood flux. We provide in the next two subsections some basic reasons that lie behind the collapse of flux in spherocytosis by illustrating the reduction of the cell-free layer and the significantly higher dispersion of spherical cells (hydrodynamics diffusion). These factors contribute to heightened resistance in the blood flow, consequently leading to a lower cellular flux.

The interplay between reduced area (τ) and channel width (see Fig. 5) can be seen as follows. RBCs traversing channels of varying widths have different abilities to deform. For example, for a channel width of $10 \mu\text{m}$, even if a RBC with reduced area 0.64 (or smaller) can deform more amply than a more inflated cell, its parachute (or slipper) shape confers to it a large enough transverse section as compared to that of a RBC with reduced area 0.82, so that its resistance to flow is significant (see top three panels in Fig. 6). This makes the cell with a large enough reduced area slightly more efficient (Fig. 2). Conversely, for a larger width (say $W = 40 \mu\text{m}$), cells with a small

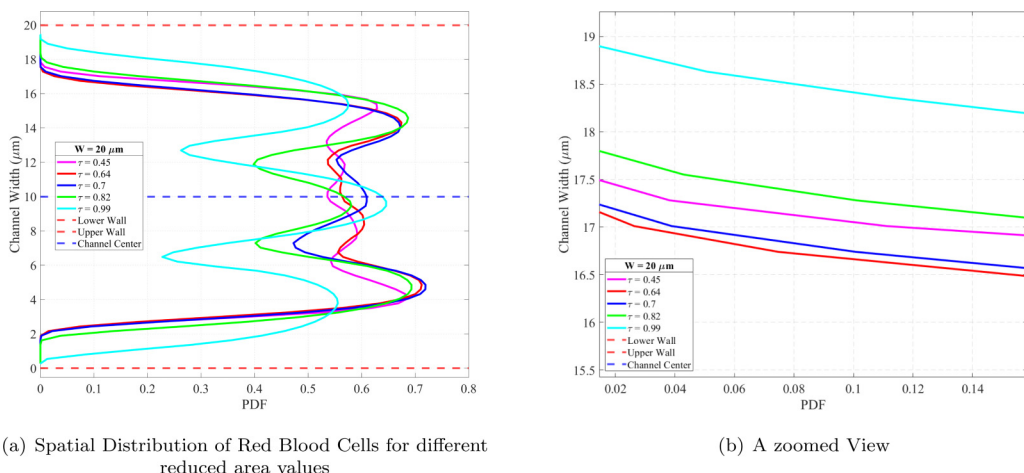


FIG. 7. Spatial distribution of red blood cells in a $20\ \mu\text{m}$ channel (RBCs with fixed area): The influence of reduced area. (a) The probability density function of RBCs for various reduced areas (0.45–0.99) in a $20\ \mu\text{m}$ channel, with a fixed hematocrit of 0.4 and $Ca = 18$. (b) A zoomed-in view showcasing the PDF of RBCs for different reduced areas.

reduced area can elongate along the flow, thus reducing the flow resistance (see three bottom panels in Fig. 6). This is why a cell with a small enough reduced area becomes favorable (see Fig. 4).

2. Cell-free layer (CFL)

The cell-free layer, often referred to as the “plasma layer” or “cell-depleted layer,” is a crucial component in microcirculation. This narrow, clear zone that lines the interior of blood vessels, particularly in capillaries and arterioles, is devoid of blood cells and primarily consists of plasma. The presence of this cell-free layer is a result of the hydrodynamic interactions between flowing blood cells and the hydrodynamic lift due to vessel wall. It plays a pivotal role in maintaining efficient blood flow by reducing frictional forces between the blood and the vessel wall [56,57].

In Fig. 7, we present the probability density function (PDF) depicting the spatial distribution of RBCs for varying reduced area values (we calculate the spatial distribution of RBCs based on their entire cell body, rather than focusing solely on the cell center to be more accurate). Let us, as a way of example, consider the case $W = 20\ \mu\text{m}$ for which the maximum flux is obtained for $\tau = 0.64$ (see Fig. 3). Our observations reveal a noteworthy trend: as the reduced area decreases, starting from a quasicircular shape, the size of CFL expands, leading to enhanced blood flux. In larger CFLs, RBCs experience less hindrance and are afforded greater freedom to migrate closer to the channel’s center. We present, in the Supplemental Material [54], the velocity profile in the presence of cells, revealing a flattened shape due to accumulation of cells in the channel center.

We have also analyzed the CFL for the other channel widths. Figure 8 shows that the optimal reduced area value associated with the highest flux (see Figs. 2–4) aligns with a thicker cell-free layer. Note that the trend may appear small in some cases (for example, for $W = 10\ \mu\text{m}$, the difference between reduced areas of 0.82 and 0.64 is about $0.3\ \mu\text{m}$) has been checked with the highest resolution we could achieve. Note also that $0.3\ \mu\text{m}$ corresponds to a relative difference of about 15–20 %, since the CFL width is about $1.5\ \mu\text{m}$. This observation sheds light on the correlation between channel width and the reduced area of RBCs: a maximal CFL is correlated with a maximal RBCs flux.

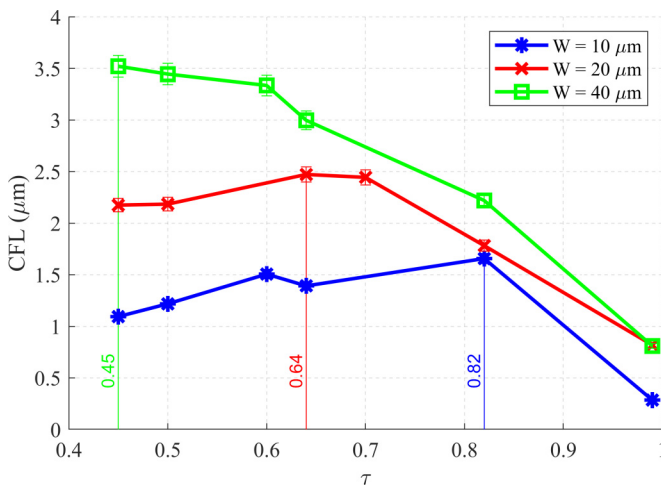


FIG. 8. Cell-free layer (CFL) versus reduced area in a 10 μm , 20 μm , and 40 μm channel widths (RBCs with fixed area): This figure demonstrates the relationship between the CFL and reduced area in different channel widths, with a constant $Ca = 18$. The vertical lines indicate the maximum CFL for corresponding values of τ , 0.45 for $W = 40 \mu\text{m}$, 0.64 for $W = 20 \mu\text{m}$, and 0.82 for $W = 10 \mu\text{m}$ (Hematocrit corresponds to the highest flux: 41% for $W = 10 \mu\text{m}$, 40% for $W = 20 \mu\text{m}$ and 30% for $W = 40 \mu\text{m}$).

3. RBCs diffusion

To quantify the spatial dispersion of a particle over time, we calculated the variance of the displacements as a measure of the distribution of individual cell displacements from the mean. The variance at time t was computed as $\text{Var}(t) = \langle (d(t) - \langle d(t) \rangle)^2 \rangle$, where $d(t)$ is displacement of a particle after time t , and $\langle d(t) \rangle$ is the mean displacement at time t . The average in the variance is a sum over all particles.

Subsequently, we calculated the diffusion coefficient (D), a measure that characterizes the rate at which the cells spread from their initial positions over time. Assuming a one-dimensional (in the y direction; this is legitimate since over a long time the flow becomes quasitranslationally invariant along the flow direction) random walk, the diffusion coefficient for a given time lag was calculated using the formula $D(\text{lag}) = \text{Var}(\text{lag}) / (\text{lag} \times dt)$, where lag dt is the elapsed time between two consecutive time intervals (lag) for which the measurement is performed. Each time frame interval is large in comparison to the computational step time, but small in comparison to the full simulation time. Typically, the time frame interval choice is motivated by the fact the cell configuration has changed by about a few percent during that time.

A large diffusion coefficient signifies an elevated degree of cellular dispersion, indicative of increased cellular mobility within the microfluidic channel. This phenomenon results in the formation of a narrower cell-free layer (refer to Fig. 8), an essential characteristic impacting blood flow dynamics, as discussed above. Conversely, a small diffusion coefficient implies restricted cellular movement in the y direction, constraining the cells closer to the central region of the channel and consequently leading to a wider CFL.

Our study reveals a clear relationship between the diffusion coefficient and blood flow, as elucidated in Fig. 9. Specifically, lower values of D are intimately associated with heightened blood flow rates. This association coincides with a thicker CFL, as demonstrated in Fig. 8, and is especially pronounced when the reduced area of red blood cells approaches the optimal value (see Fig. 5), signifying a decreased cellular dispersion within the channel. High D values yield a thinner CFL, often correlated with a reduced area value of 0.99, resulting in a markedly reduced blood flow rate.

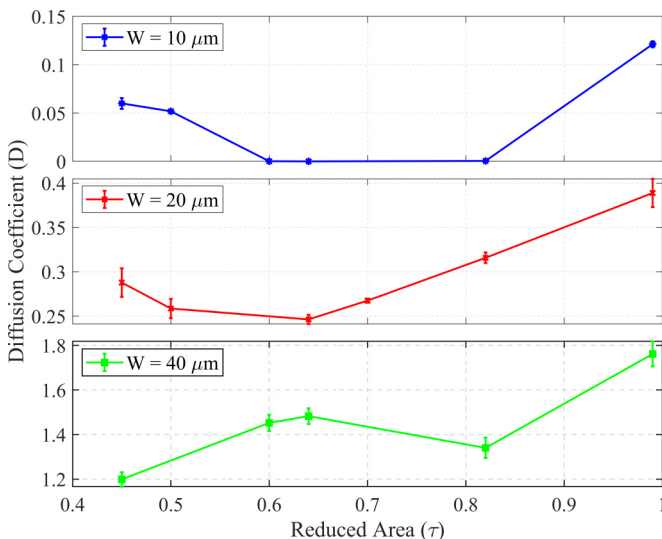


FIG. 9. Diffusion coefficient versus the reduced areas: The lower diffusion corresponds to the higher flux value (RBCs with fixed area): In a $10\ \mu\text{m}$ ($Cn = 0.54$) channel, for a hematocrit of 0.4, where we have the higher flux; in a $20\ \mu\text{m}$ ($Cn = 0.27$) Channel, for a hematocrit of 0.4, where we have the higher flux; and in a $40\ \mu\text{m}$ ($Cn = 0.14$) channel, for a hematocrit of 0.3, where we have the higher flux.

Notably, the lower D values consistently yield maximum blood flux across the range of channel widths studied.

4. Optimal flux values

In this section, we present optimal values derived from our numerical investigation. Figure 10 presents the maximal flux as a function of the reduced area, discerning various studied channel widths. Notably, our analysis reveals that within a channel width of $40\ \mu\text{m}$, the maximum of blood

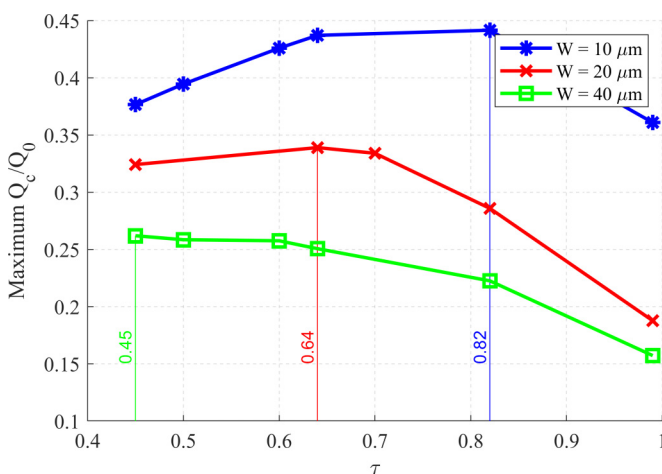


FIG. 10. Maximum flux for studied reduced areas in different channel widths: This figure displays the corresponding maximum flux for each of the reduced areas studied (Hematocrit of 41% for $W = 10\ \mu\text{m}$, 40% for $W = 20\ \mu\text{m}$, and 30% for $W = 40\ \mu\text{m}$), in channels with widths of $10\ \mu\text{m}$, $20\ \mu\text{m}$, and $40\ \mu\text{m}$ (RBCs with fixed area).

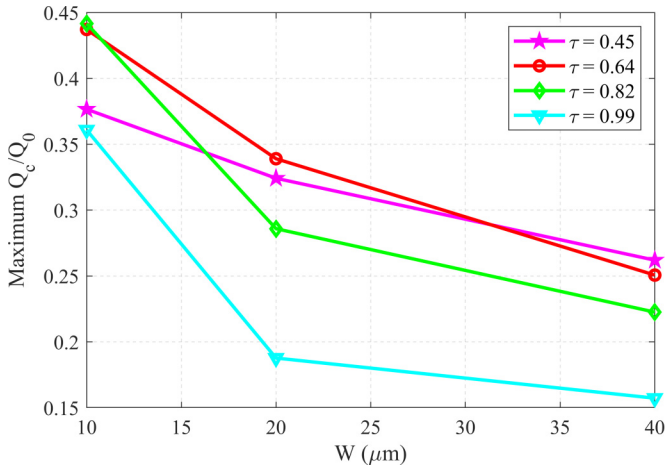


FIG. 11. Optimal flux versus Channel width for different reduced areas: This figure shows the relationship between the optimal flux and channel width for various reduced areas of 0.45, 0.64, 0.82, and 0.99 (RBCs with fixed area).

flux is achieved at a reduced area value of about 0.45. Conversely, when the channel width is reduced to $10 \mu\text{m}$, the blood flux is optimal for a reduced area of about 0.82.

Furthermore, Fig. 11 shows the multifaceted dependency of maximum blood flux on both the reduced area and channel width. For instance, a reduced area of 0.99 yields a maximum blood flux (dimensionalized by Q_0) of approximately 0.36, whereas a channel width of $20 \mu\text{m}$ corresponds to a reduced blood flux of approximately 0.19.

Figure 12 supplements our analysis by shedding light on the optimal hematocrit levels that correlate with the highest attainable blood flux. In the context of a $40 \mu\text{m}$ channel width, our findings indicate that the optimal hematocrit concentration, which results in maximum blood flux, is about

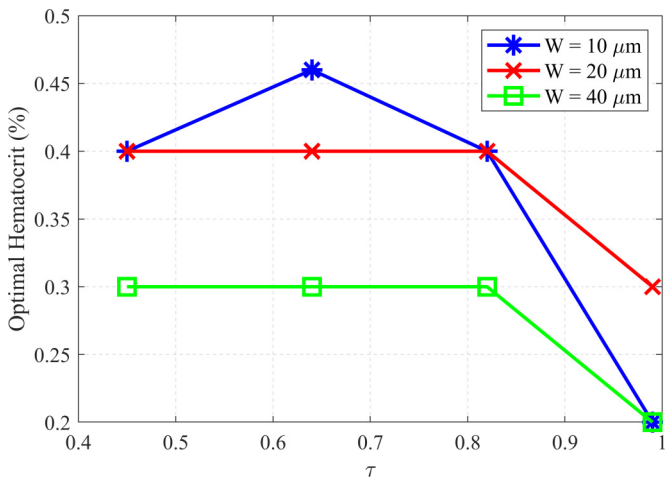


FIG. 12. Optimal volume fraction for maximum RBCs flux versus reduced area in different channel widths [$10 \mu\text{m}$ ($Cn = 0.54$), $20 \mu\text{m}$ ($Cn = 0.27$), and $40 \mu\text{m}$ ($Cn = 0.14$)]: This figure illustrates the optimal volume fraction where the highest RBCs flux is achieved, as a function of the reduced area for three distinct channel widths of $10 \mu\text{m}$, $20 \mu\text{m}$, and $40 \mu\text{m}$ (RBCs with fixed area).

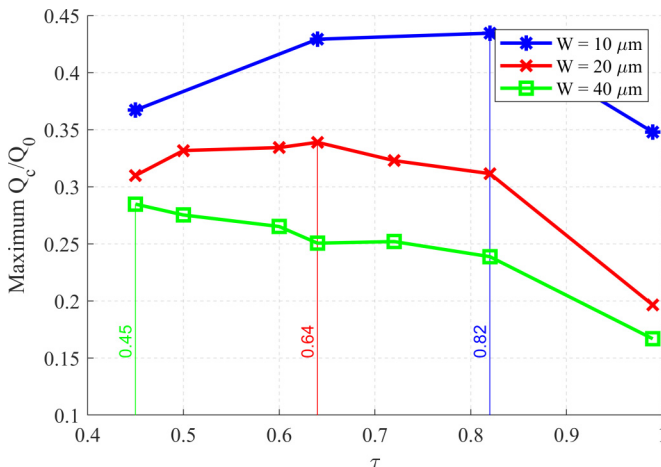


FIG. 13. Maximum flux for studied reduced areas in different channel widths (RBCs with fixed perimeter).

0.3 for all explored reduced area values, except for spherical cells where it decreases to about 0.2. In the case of a $20 \mu\text{m}$ channel width, the optimal hematocrit level is approximately 0.4, with the exception of spherical cells, which plateau at 0.3.

B. Red blood cells with fixed perimeter

Abnormal shapes (like spherocytosis and ellipsocytosis) have different volumes and/or different areas as compared to healthy shapes [6,11,58,59]. In the previous section, we have assumed that the analog of volume (enclosed area in 2D) is fixed and the perimeter is varied. Here we will fix the cell's perimeter, and vary the cell's area, in order to achieve a desired reduced area. Our primary objective is to investigate whether alterations in either the cell's area or perimeter within the same confinement would yield distinct outcomes.

The main results are presented in Fig. 13. When we compare these results with those obtained from our previous simulation in the previous section, where the cell's area was kept constant (Fig. 10), a notable consistency emerges. It becomes evident that the optimal reduced area remains quasiinvariant across different channel widths, suggesting a consistent relation.

From our findings, it can be inferred that the RBC's shape and deformability are central to its interaction with the surrounding environment and, consequently, its ability to navigate through narrow channels. The consistency of optimal reduced areas across various channel widths implies that the cell's morphology and deformability might play a more critical role than its specific geometric parameters (area or perimeter) in influencing blood flow behavior.

IV. CONCLUSIONS

In summary, our investigation has yielded some insights into the intricate relationship between channel dimensions and the optimal reduced area regarding the RBCs flux. Additionally, our investigation led to the fact that the cell-free layer (CFL) and the diffusion coefficient are correlated with optimal flow.

These findings offer a deeper understanding of the hemodynamic implications of RBC morphological anomalies. We have shown, in particular, that a reduced area close to one (the case of spherocytosis) leads to a collapse of RBCs flux, attaining up to 50%. This should severely compromise oxygen and other metabolites transport in microcirculation.

Several questions deserve future consideration. First, our study has a limitation since it is focused on a 2D situation. While several studies (including ours) [44–47] had reported on similarities of

behaviors in 2D and 3D, a systematic analysis of 3D flow is necessary. Second, we have found that the optimal reduced area depends on channel width. Since in real vascular networks, different vessels have different diameters, it is not yet clear how our findings can be translated to real microvasculatures. A systematic study of blood flow in complex geometry is necessary in order to build a clear conclusion about the impact of shape abnormalities on blood flow transport. It is hoped to investigate these questions in future work.

ACKNOWLEDGMENTS

M.B., M.A., and C.M. thank CNES (Centre National d'Etudes Spatiales) for financial support and for access to microgravity data. C.W. and M.B. acknowledge funding from the DFG Project No. WA1336/12-2. All the authors thank the French-German university programme "Living Fluids" (Grant No. CFDA-Q1-14) for financial support.

- [1] G. Mchedlishvili and N. Maeda, Blood flow structure related to red cell flow: determinant of blood fluidity in narrow microvessels, *Jpn. J. Physiol.* **51**, 19 (2001).
- [2] S. Chien, Red cell deformability and its relevance to blood flow, *Annu. Rev. Physiol.* **49**, 177 (1987).
- [3] A. Berzuini, C. Bianco, A. C. Migliorini, M. Maggioni, L. Valenti, and D. Prati, Red blood cell morphology in patients with covid-19-related anaemia, *Blood Transfus.* **19**, 34 (2021).
- [4] D. Gérard, S. Ben Brahim, J. F. Lesesve, and J. Perrin, Are mushroom-shaped erythrocytes an indicator of covid-19? *Br. J. Haematol.* **192**, 230 (2021).
- [5] A. Iolascon, R. Avvisati, and C. Piscopo, Hereditary spherocytosis, *Transfus. Clin. Biol.* **17**, 138 (2010), "Role of blood group antigens and associated molecules in red cell biology: from molecular approach to clinical applications" organized by Institut National de la Transfusion Sanguine, September 15th to 17th 2010.
- [6] L. Da Costa, J. Galimand, O. Fenneteau, and N. Mohandas, Hereditary spherocytosis, elliptocytosis, and other red cell membrane disorders, *Blood Reviews* **27**, 167 (2013).
- [7] E. Schapkaitz and M. H. Mezgebe, The clinical significance of schistocytes: a prospective evaluation of the international council for standardization in hematology schistocyte guidelines, *Turk. J. Hematol.* **34**, 59 (2017).
- [8] P. G. Gallagher, 164 - hemolytic anemias: Red cell membrane and metabolic defects, in *Goldman's Cecil Medicine (Twenty Fourth Edition)*, edited by L. Goldman and A. I. Schafer (W.B. Saunders, Philadelphia, 2012), pp. 1052–1060
- [9] A. L. Montoya-Navarrete, A. L. Guerrero-Barrera, T. Quezada-Tristán, A. G. Valdivia-Flores, and M. J. Cano-Rábano, Red blood cells morphology and morphometry in adult, senior, and geriatricians dogs by optical and scanning electron microscopy, *Front. Vet. Sci.* **9**, 998438 (2022).
- [10] D. Flormann, M. Qiao, N. Murciano, I. Giulia, A. Darras, S. Hof, S. M. Recktenwald, M. G. Rotordam, N. Becker, J. Geisel *et al.*, Transient receptor potential channel vanilloid type 2 in red cells of cannabis consumer, *American J. Hematol.* **97**, E180 (2022).
- [11] G. Tomaiuolo, Biomechanical properties of red blood cells in health and disease towards microfluidics, *Biomicrofluidics* **8**, 051501 (2014).
- [12] F. C. Mokken, M. Kedaria, C. P. Henny, M. Hardeman, and A. Gelb, The clinical importance of erythrocyte deformability, a hemorrheological parameter, *Ann. Hematol.* **64**, 113 (1992).
- [13] T. W. Secomb, Blood flow in the microcirculation, *Annu. Rev. Fluid Mech.* **49**, 443 (2017).
- [14] G. Mchedlishvili, Disturbed blood flow structuring as critical factor of hemorrheological disorders in microcirculation, *Clin. Hemorheol. Microcirc.* **19**, 315 (1998).
- [15] D. Cordasco and P. Bagchi, On the shape memory of red blood cells, *Phys. Fluids* **29**, 041901 (2017).
- [16] D. Cordasco, A. Yazdani, and P. Bagchi, Comparison of erythrocyte dynamics in shear flow under different stress-free configurations, *Phys. Fluids* **26**, 041902 (2014).

- [17] M. Alafzadeh, S. Yaghoubi, E. Shirani, and M. Rahmani, Simulation of rbc dynamics using combined low dimension, immersed boundary and lattice boltzmann methods, *Mol. Simul.* **49**, 1179 (2023).
- [18] H. Zhao and E. S. Shaqfeh, The dynamics of a vesicle in simple shear flow, *J. Fluid Mech.* **674**, 578 (2011).
- [19] Z. Peng, O. S. Pak, Z. Feng, A. P. Liu, and Y.-N. Young, On the gating of mechanosensitive channels by fluid shear stress, *Acta Mechanica Sinica* **32**, 1012 (2016).
- [20] S. K. Veerapaneni, Y.-N. Young, P. M. Vlahovska, and J. Bławdziewicz, Dynamics of a compound vesicle in shear flow, *Phys. Rev. Lett.* **106**, 158103 (2011).
- [21] B. Kaoui, G. Biros, and C. Misbah, Why do red blood cells have asymmetric shapes even in a symmetric flow? *Phys. Rev. Lett.* **103**, 188101 (2009).
- [22] G. Kabacaoğlu and G. Biros, Sorting same-size red blood cells in deep deterministic lateral displacement devices, *J. Fluid Mech.* **859**, 433 (2019).
- [23] D. A. Fedosov, B. Caswell, and G. E. Karniadakis, A multiscale red blood cell model with accurate mechanics, rheology, and dynamics, *Biophys. J.* **98**, 2215 (2010).
- [24] F. Sotiropoulos, C. Aidun, I. Borazjani, and R. MacMeccan, Computational techniques for biological fluids: from blood vessel scale to blood cells, *Image-Based Computational Modeling of the Human Circulatory and Pulmonary Systems: Methods and Applications*, 105 (2011).
- [25] D. A. Reasor Jr, J. R. Clausen, and C. K. Aidun, Coupling the lattice-boltzmann and spectrin-link methods for the direct numerical simulation of cellular blood flow, *Int. J. Numer. Methods Fluids* **68**, 767 (2012).
- [26] A. Guckenberger, A. Kihm, T. John, C. Wagner, and S. Gekle, Numerical–experimental observation of shape bistability of red blood cells flowing in a microchannel, *Soft Matter* **14**, 2032 (2018).
- [27] A. Nait-Ouhra, A. Guckenberger, A. Farutin, H. Ez-Zahraouy, A. Benyoussef, S. Gekle, and C. Misbah, Lateral vesicle migration in a bounded shear flow: Viscosity contrast leads to off-centered solutions, *Phys. Rev. Fluids* **3**, 123601 (2018).
- [28] T. Krüger, M. Gross, D. Raabe, and F. Varnik, Crossover from tumbling to tank-treading-like motion in dense simulated suspensions of red blood cells, *Soft Matter* **9**, 9008 (2013).
- [29] Y. Rashidi, G. Simionato, Q. Zhou, T. John, A. Kihm, M. Bendaoud, T. Krüger, M. O. Bernabeu, L. Kaestner, M. W. Laschke *et al.*, Red blood cell lingering modulates hematocrit distribution in the microcirculation, *Biophys. J.* **122**, 1526 (2023).
- [30] T. M. Fischer, Shape memory of human red blood cells, *Biophys. J.* **86**, 3304 (2004).
- [31] T. M. Fischer, The shape of human red blood cells suspended in autologous plasma and serum, *Cells* **11**, 1941 (2022).
- [32] J. Mauer, S. Mendez, L. Lanotte, F. Nicoud, M. Abkarian, G. Gompper, and D. A. Fedosov, Flow-induced transitions of red blood cell shapes under shear, *Phys. Rev. Lett.* **121**, 118103 (2018).
- [33] S. Mendez and M. Abkarian, Single red blood cell dynamics in shear flow and its role in hemorheology, in *Dynamics of Blood Cell Suspensions in Microflows* (CRC Press, Boca Raton, 2019) pp. 125–182.
- [34] M. Abkarian, M. Faivre, and A. Viallat, Swinging of red blood cells under shear flow, *Phys. Rev. Lett.* **98**, 188302 (2007).
- [35] M. Nouaman, A. Darras, T. John, G. Simionato, M. A. Rab, R. van Wijk, M. W. Laschke, L. Kaestner, C. Wagner, and S. M. Recktenwald, Effect of cell age and membrane rigidity on red blood cell shape in capillary flow, *Cells* **12**, 1529 (2023).
- [36] S. M. Recktenwald, K. Graessel, F. M. Maurer, T. John, S. Gekle, and C. Wagner, Red blood cell shape transitions and dynamics in time-dependent capillary flows, *Biophys. J.* **121**, 23 (2022).
- [37] A. Kumar, R. G. H. Rivera, and M. D. Graham, Flow-induced segregation in confined multicomponent suspensions: effects of particle size and rigidity, *J. Fluid Mech.* **738**, 423 (2014).
- [38] B. Kaoui and J. Harting, Two-dimensional lattice boltzmann simulations of vesicles with viscosity contrast, *Rheol. Acta* **55**, 465 (2016).
- [39] Z. Shen, A. Farutin, M. Thiébaud, and C. Misbah, Interaction and rheology of vesicle suspensions in confined shear flow, *Phys. Rev. Fluids* **2**, 103101 (2017).
- [40] T. Krüger, F. Varnik, and D. Raabe, Efficient and accurate simulations of deformable particles immersed in a fluid using a combined immersed boundary lattice boltzmann finite element method, *Computers & Mathematics with Applications* **61**, 3485 (2011).

- [41] Z. Shen, G. Couplier, B. Kaoui, B. Polack, J. Harting, C. Misbah, and T. Podgorski, Inversion of hematocrit partition at microfluidic bifurcations, *Microvasc. Res.* **105**, 40 (2016).
- [42] B. Kaoui, R. J. Jonk, and J. Harting, Interplay between microdynamics and macrorheology in vesicle suspensions, *Soft Matter* **10**, 4735 (2014).
- [43] B. Kaoui, J. Harting, and C. Misbah, Two-dimensional vesicle dynamics under shear flow: Effect of confinement, *Phys. Rev. E* **83**, 066319 (2011).
- [44] M. Thiébaud, Z. Shen, J. Harting, and C. Misbah, Prediction of anomalous blood viscosity in confined shear flow, *Phys. Rev. Lett.* **112**, 238304 (2014).
- [45] D. A. Fedosov, M. Peltomäki, and G. Gompper, Deformation and dynamics of red blood cells in flow through cylindrical microchannels, *Soft Matter* **10**, 4258 (2014).
- [46] S. Quint, A. Christ, A. Guckenberger, S. Himbert, L. Kaestner, S. Gekle, and C. Wagner, 3d tomography of cells in micro-channels, *Appl. Phys. Lett.* **111**, 103701 (2017).
- [47] A. Farutin, Z. Shen, G. Prado, V. Audemar, H. Ez-Zahraouy, A. Benyoussef, B. Polack, J. Harting, P. M. Vlahovska, T. Podgorski *et al.*, Optimal cell transport in straight channels and networks, *Phys. Rev. Fluids* **3**, 103603 (2018).
- [48] M. Abbasi, A. Farutin, H. Ez-Zahraouy, A. Benyoussef, and C. Misbah, Erythrocyte-erythrocyte aggregation dynamics under shear flow, *Phys. Rev. Fluids* **6**, 023602 (2021).
- [49] B. Kaoui, G. H. Ristow, I. Cantat, C. Misbah, and W. Zimmermann, Lateral migration of a two-dimensional vesicle in unbounded poiseuille flow, *Phys. Rev. E* **77**, 021903 (2008).
- [50] T. Krüger, S. Frijters, F. Günther, B. Kaoui, and J. Harting, Numerical simulations of complex fluid-fluid interface dynamics, *Eur. Phys. J.: Spec. Top.* **222**, 177 (2013).
- [51] H. Zhang, Z. Shen, B. Hogan, A. I. Barakat, and C. Misbah, ATP release by red blood cells under flow: model and simulations, *Biophys. J.* **115**, 2218 (2018).
- [52] N. Takeishi, M. E. Rosti, Y. Imai, S. Wada, and L. Brandt, Haemorheology in dilute, semi-dilute and dense suspensions of red blood cells, *J. Fluid Mech.* **872**, 818 (2019).
- [53] T. Krüger, H. Kusumaatmaja, A. Kuzmin, O. Shardt, G. Silva, and E. M. Viggen, The lattice boltzmann method, graduate texts in physics (2017).
- [54] See Supplemental Material at <http://link.aps.org/supplemental/10.1103/PhysRevFluids.9.053603> for varying rigidities of RBCs and different viscosity contrasts.
- [55] M. Thiébaud and C. Misbah, Rheology of a vesicle suspension with finite concentration: A numerical study, *Phys. Rev. E* **88**, 062707 (2013).
- [56] Y. Rashidi, O. Aouane, A. Darras, T. John, J. Harting, C. Wagner, and S. M. Recktenwald, Cell-free layer development and spatial organization of healthy and rigid red blood cells in a microfluidic bifurcation, *Soft Matter* **19**, 6255 (2023).
- [57] S. M. Recktenwald, K. Graessel, Y. Rashidi, J. N. Steuer, T. John, S. Gekle, and C. Wagner, Cell-free layer of red blood cells in a constricted microfluidic channel under steady and time-dependent flow conditions, *Phys. Rev. Fluids* **8**, 074202 (2023).
- [58] N. M. Geekiyanage, M. A. Balanant, E. Sauret, S. Saha, R. Flower, C. T. Lim, and Y. Gu, A coarse-grained red blood cell membrane model to study stomatocyte-discocyte-echinocyte morphologies, *PLoS One* **14**, e0215447 (2019).
- [59] K. Khairy, J. Foo, and J. Howard, Shapes of red blood cells: comparison of 3d confocal images with the bilayer-couple model, *Cel. Mol. Bioeng.* **1**, 173 (2008).